CHEMISTRY OF MATERIALS

ARTICLE

pubs.acs.org/cm

Single-Step Aerosol Synthesis and Deposition of Au Nanoparticles with Controlled Size and Separation Distributions

Elijah Thimsen

Institute of Chemical Sciences and Engineering, Ecole Polytechnique Fédérale de Lausanne, Lausanne, Switzerland

Supporting Information

ABSTRACT: Immobilized noble metal nanoparticles are being explored for a variety of applications where control over the particle size and separation distance on the substrate is important for performance. A proof of concept is presented that Au nanoparticles can be deposited in a single step with control over the size and separation distributions using an aerosol process. Samples were deposited with mean particle diameters in the range from 15 to 43 nm, and mean separation distances from 11 to 39 nm. Depending on the separation distance, particles exhibited localized surface plasmon resonance dominated by either intra- or interparticle resonances, as determined by ultraviolet−visible extinction spectroscopy. Ultrathin TiO_2 shells of different thicknesses, in the range from 0 to 24 nm, were deposited on the Au nanoparticles by atomic layer deposition to determine the sensing distance into the surrounding dielectric medium for these materials, which was estimated to be 10 nm.

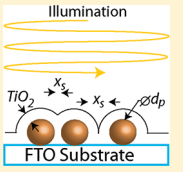

KEYWORDS: aerosol, Au nanoparticle, localized surface plasmon resonance, atomic layer deposition, TiO_2, flame synthesis

INTRODUCTION

Noble metal nanostructures have drawn attention for more than a century because of the interesting optical properties that emerge as the characteristic size of the structure becomes less than the wavelength of the incident photon.[1] Recently, many applications have been explored for these plasmonic materials, including surface-enhanced Raman spectroscopy (SERS),[2−6] detection of molecular adsorption,[7] intense nanolocalized heating,[8] plasmon-enhanced solar cells,[9] and plasmon-enhanced photoelectrochemical water splitting.[10]

One of the most active geometries consists of metal nanoparticles immobilized on a substrate. This geometry has produced one of the highest SERS signals to date, resulting in a signal enhancement factor of 10^{14} at certain hot spots,[2] elevating SERS to the level of single molecule sensitivity. In comparison to nanoparticles immobilized on a substrate, typical values reported for nanostructures produced by lithographic techniques have often resulted in lower SERS enhancement factors from 10^4 to 10^9.[3−5] The field enhancement in the gap between two nanoparticles is dramatically larger than for isolated particles, and is a strong function of particle size and interparticle separation, with greater enhancements for larger diameters (60 nm) separated by smaller distances (1 to 6 nm).[6] It is clear that processes for the synthesis of plasmonic nanostructures must offer simultaneous control over particle size and separation to fully realize applications. Synthesis processes must also be amenable to scale up.

While many processes have been explored for the synthesis of noble metal nanoparticles immobilized on substrates, existing methods either do not offer a uniform deposit with rational control over size and the separation distance while affording a clean particle surface free of reaction byproducts or are multistep, complicated, and not amenable to scale-up. For instance, great strides have been made in colloidal nanoparticle self-assembly,[11−13] and control over particle spacing in superlattices and other structures can be achieved through judicious selection of the organic surface ligands;[11] but it is still early days for the application of such materials and not clear if the performance and ease of processing will promote these structures to ubiquity. Because of the diversity of different application requirements, there is a need for alternative synthesis routes to immobilized nanoparticle structures with controlled characteristics. Aerosol deposition offers an attractive bottom-up alternative for synthesis and deposition of nanoparticles in a single processing step. Aerosol processing can be scaled up to make industrially relevant quantities of both functional powders and highly uniform solids.[14,15] Control over particle size and aggregation state in the aerosol can be achieved through judicious selection of process parameters,[16−19] and the interparticle separation on the substrate can be controlled through the deposition time in the early stages of film growth.[20,21] Relatively little work has been done on aerosol synthesis and deposition of plasmonic noble metal nanostructures at atmospheric pressure. There have been a few reports on the incorporation of Au and Ag nanoparticles into ceramic nanocomposites via aerosol routes[22−25] and incorporation of Cu into carbon composites for relative humidity sensing,[26] but this area is largely unexplored. Development of aerosol processes for the synthesis of plasmonic materials could be of great benefit for realizing high performance in applications, and also for improving the fundamental understanding of deposition processes and particle interactions.

In this report, a proof of concept is presented that Au nanoparticles immobilized on a substrate with controlled size and separation distance can be synthesized in a single step using an atmospheric pressure flame aerosol reactor (FLAR). The FLAR was used to deposit samples where the localized surface plasmon resonance (LSPR) was dominated by either intra- or interparticle resonances. Ultrathin TiO_2 shells were deposited onto the Au nanoparticles by atomic layer deposition (ALD) with

Received: August 1, 2011
Published: September 27, 2011

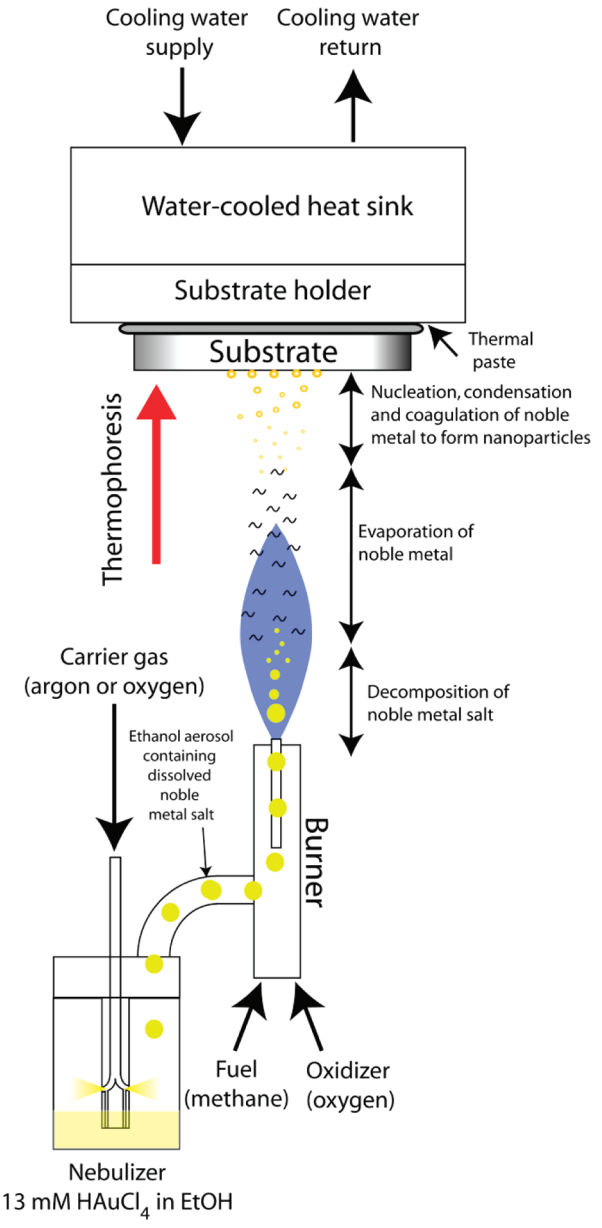

Figure 1. Schematic of the flame aerosol reactor (FLAR).

precisely controlled thickness at the nanometer length scale using the standard titanium tetra-isopropoxide (TTIP) and water process. Atomic layer deposition (ALD) is a well-established, reliable process for the deposition of conformal films on nanostructured substrates. For instance, the TTIP/H_2O process has been used to coat porous aerogel substrates that had a tortuous morphology with an average pore size of 20 nm and an overall thickness of 25 μm.[27] For coating metals, there is precedence in the literature for the TTIP/H_2O process forming conformal films on Ag nanoparticles supported by FTO.[9,28] The sensing distance, which is an estimate of the distance the photoexcited electromagnetic field penetrates into the surrounding dielectric medium,[28,29] is important for estimating the distance dependence of photocurrent enhancement in plasmon-enhanced solar cells,[9] and also for estimating the sampling volume for plasmon-based sensors. The sensing distance for the materials presented herein was determined for different nanostructures from the extinction spectra as a function of TiO_2 shell thickness.

RESULTS AND DISCUSSION

Synthesis. The atmospheric pressure FLAR used in this study to synthesize the immobilized Au nanoparticles was similar to the reactor previously reported[17,18,30] but had a modified precursor feeding system. A schematic of the reactor is presented in Figure 1. The bubbler of the standard system was replaced with a nebulizer. At the nebulizer supply pressure used for this work, the manufacturer's reported mass mean diameter (MMD) of the $HAuCl_4$-containing ethanol droplets generated by the spray was 5.8 μm with a geometric standard deviation of 1.78. The following mechanism is proposed. It is assumed that the ethanol in the nebulized aerosol evaporated, leaving behind $HAuCl_4$ residue particles. On the basis of the $HAuCl_4$ concentration and MMD of the nebulized aerosol, the residue particles were approximately 610 nm in diameter when fed into the flame. At the relatively high temperature in the flame (~2200 K), the Au^{3+} was reduced to Au by thermal decomposition, which was likely present initially as particles with a maximum size of approximately 510 nm in diameter, assuming Au was conserved while chlorine was volatilized either as HCl or Cl_2, which could have resulted in fragmentation and a smaller initial particle diameter. Au_2O_3 will not form because it is a very unstable material. With use of the kinetic data provided by Tsai et al.,[31] the calculated time constant of the first-order decomposition reaction of Au_2O_3 to form 2Au and $^3/_2O_2$ is 2.0 times shorter than the lower limit of the residence time in the luminous portion of the flame (see Supporting Information).

Still in the hot, luminous region of the flame, the saturation ratio of Au was 1.8×10^{-3} ($P_{Au} = 7.9 \times 10^{-6}$ atm estimated from the Au feed rate of 1.2 μmol min^{-1} and a total gas flow rate of 3.7 lpm, vapor pressure of Au calculated at 2200 K), so there was a strong driving force for the Au particles to evaporate and form Au vapor. The temperature distribution and evolution of the saturation ratio after the flame are presented in Figure S1. The Au vapor remained undersaturated ($S_R = P_{Au}/P_{Au,sat} < 1$) until approximately 9.5 cm above the burner outlet (Figure S1), after which the Au vapor became supersaturated, resulting in homogeneous nucleation and condensation to form nanoparticles. The newly formed nuclei underwent a coagulation growth process (assuming rapid sintering) and were deposited by thermophoresis via an individual particle deposition (IPD) process.[17,19] There was a negligible amount of surface oxide on the Au as evidenced by the stability of the peak LSPR wavelength upon annealing (see Supporting Information).

The size of the Au nanoparticles as they arrive at the substrate can be controlled by a variety of process parameters. Common parameters are the residence time and precursor concentration.[16−19] Here it was found that the gas makeup can also be used to tune the particle size, where particles formed using oxygen as the nebulizer carrier gas were larger and particles formed using argon as the nebulizer carrier gas were smaller (Figure 2). This effect presumably resulted from the influence of the makeup gas on the flame temperature (argon having a lower heat capacity and therefore higher adiabatic flame temperature) and the subsequent condensation and coagulation dynamics.[32,33]

The separation of the nanoparticles on the substrate (F:SnO_2, FTO) was controlled through the deposition time during the initial stages of growth. The particle separation is presented as a distribution because each particle had several neighbors, some at different separations, and therefore the separation was a distributed random variable with associated distribution parameters.

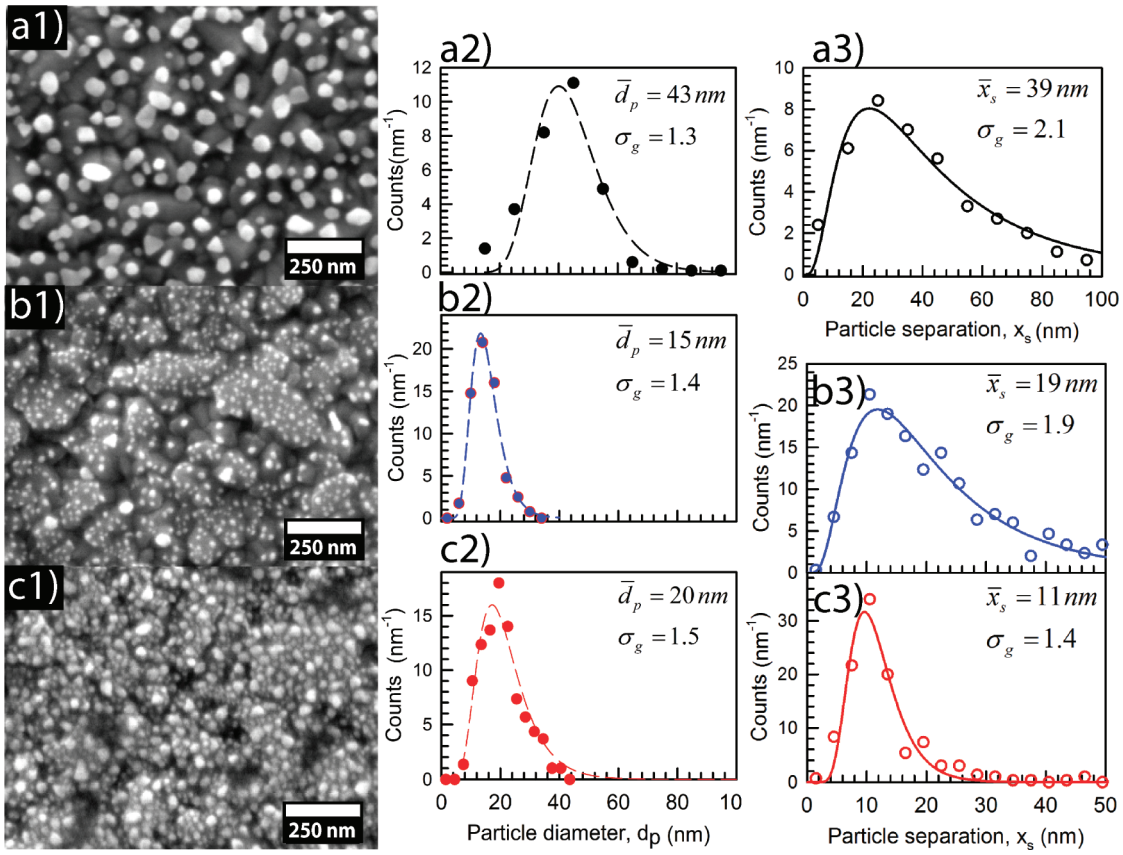

Figure 2. Plan-view SEM images (a1, b1, and c1), particle size (a2, b2, and c2), and separation (a3, b3, and c3) distributions. The distribution mean ($\bar{d}_p$) and geometric standard deviation (σ_g) of the size distributions are given in the insets of the middle column, whereas the mean ($\bar{x}_s$) and geometric standard deviation (σ_g) of the separation distributions are given in the insets of the right column. Note the different scale of the *x*-axis for panel a3. The experimental conditions were as follows: oxygen carrier gas, 5 min deposition time (a1, a2 and a3); argon carrier gas, 4 min deposition time (b1, b2, and b3); and argon carrier gas, 8 min deposition time (c1, c2, and c3).

For LSPR coupling between particle pairs, the interaction exponentially decreases with increasing particle separation.[34] Only the closest particles were considered because the interaction is strongest between them compared to particles farther away. The separation distribution was determined by measuring the distance from scanning electron microscope (SEM) images between the closest points on adjacent particles such that the line never passed through a particle. The distribution of distances measured in this way is the separation distribution plotted in Figure 2a3, 2b3, and 2c3. Such measurements provide the ensemble particle separation distribution, which is the relevant parameter to compare to the macroscopic extinction measurements. For the 15 nm particles deposited using argon as the carrier gas, in Figure 2b3 and 2c3, it can be seen that as the deposition time went from 4 to 8 min, the number-mean particle separation decreased from 19 to 11 nm, which was accompanied by a slight increase of number-mean particle diameter from 15 to 20 nm (Figures 2b2 and 2c2). The moderate increase in particle diameter indicated that, for the present system, the deposition time-dependent particle separation distance was not completely independent of particle diameter, which could have been a result of a small number of particles depositing on already deposited particles that sintered on the substrate to form larger particles as the deposition time went from 4 to 8 min. If the deposition time was further increased, the particles began depositing on top of one another and the deposit started growing away from the substrate, as expected from what is known in other experimental systems[17,18,35] and computational modeling.[20,21]

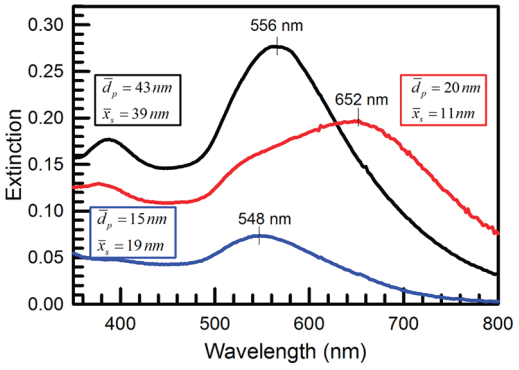

Figure 3. UV−vis extinction spectra of the as-deposited Au nanoparticles with different particle sizes and separations. The means of the size and separation distributions, $\bar{d}_p$ and $\bar{x}_s$, respectively, are given in the color-coded boxes next to the curves.

It is noted that the roughness of the substrate introduces a systematic error in the magnitude of the three-dimensional (3D) particle separation vector as measured from the two-dimensional (2D) SEM images. If one takes the rms roughness of the FTO substrate (10.2 nm) as an estimate of the vertical displacement between adjacent particles, the uncertainty in the magnitude of

dx.doi.org/10.1021/cm2022467 |*Chem. Mater.* 2011, 23, 4612–4617

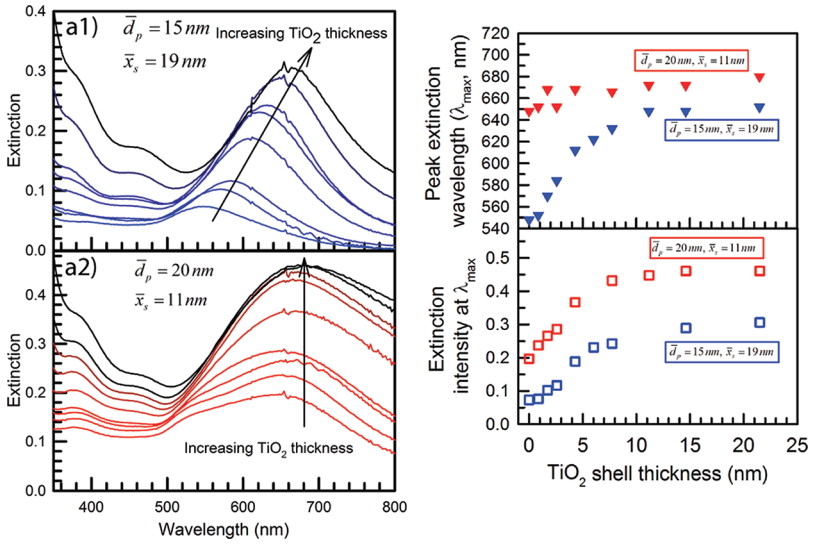

Figure 4. UV−vis extinction spectra (left column) and evolution of the peak wavelength and extinction intensity at peak wavelength (right column) of Au particles on FTO with different particle separation distributions as a function of TiO_2 shell thickness. The means of the size and separation distributions, $\bar{d}_p$ and $\bar{x}_s$, respectively, are given in the color-coded boxes in the insets of the left column and next to the respective curves of the right column. The TiO_2 was deposited in increments and the UV−vis extinction spectra were acquired between each deposition.

the 3D particle separation vector as measured from the 2D SEM images is +3% for the $\bar{x}_s$ = 39 nm case, +13% for the $\bar{x}_s$ = 19 nm case, and +36% for the $\bar{x}_s$ = 11 nm case. The author notes that FTO is a very technologically relevant substrate, and is particularly attractive in thin film and dye-sensitized solar cell applications because of its robustness during processing and low cost of manufacture.

Effect of Size and Separation on LSPR. Both the particle size and separation had a significant effect on the LSPR, as measured by UV−vis extinction spectroscopy. The UV−vis extinction spectra of the as-deposited samples are presented in Figure 3. The 15 nm particles with an average separation of 19 nm had a peak LSPR wavelength of λ_{max} = 548 nm. This value is in the expected range for isolated immobilized Au nanoparticles,[34] considering the LSPR wavelength depends on the size,[36] the shape,[6] and the dielectric environment.[10] The 43 nm particles with an average separation of 39 nm had a much larger extinction coefficient with respect to the smaller particles, and a slightly red-shifted LSPR peak wavelength of λ_{max} = 556 nm, as expected for the larger size.[36] For the 20 nm particles with an average separation of 11 nm, the LSPR was clearly dominated by inter-particle interactions, as evidenced by the broadening and red shift of the peak wavelength to λ_{max} = 652 nm. The 11 nm separation distance could have been an overestimation because the resolution of the SEM was approximately 1 nm, which may have resulted in a systematic shift of the measured distribution to larger separation values with respect to the true distribution. The broadening of the spectra for cluster matter with decreasing particle separation has been studied before for random topologies,[1] and is a result of the distribution of separation values. Each separation in the distribution induces a different red shift, producing a new extinction spectrum that is the original spectrum shifted by the separation distribution.[1] It was clear from the extinction spectra that the LSPR mode, dominated by intra- or interparticle resonances, could be readily controlled through the process parameters (i.e., deposition time) through the effect on particle separation.

Effect of TiO_2 Shell on LSPR. The LSPR mode influenced the frequency response to different dielectric environments. Ultrathin layers of amorphous TiO_2 were deposited in increments on the surface of the Au nanoparticles by ALD, which is a robust process that can be used to coat noble metal nanoparticles with conformal layers.[9,28] The deposition conditions used in this work were within the ALD window and chosen using the equipment manufacturer's recommendations. The shifts in the UV−vis extinction spectra with increasing TiO_2 shell thickness are presented in Figure 4. The samples exhibited an increase in extinction at wavelengths less than 400 nm with increasing TiO_2 thickness due to band gap excitation of the TiO_2. For the LSPR dominated by intraparticle resonances ($\bar{d}_p$ = 15 nm, $\bar{x}_s$ = 19 nm), the spectra red-shifted and the extinction increased in magnitude, as expected.[10] A mere 2.0 nm of TiO_2 was readily detected for the 15 nm particles spaced 19 nm apart, which resulted in a shift in the peak LSPR wavelength from λ_{max}= 548 nm to λ_{max}= 570 nm. After 10 nm of TiO_2 on the Au particle surface, the wavelength shift saturated and the peak position remained approximately constant at λ_{max} = 648 nm. The peak wavelength for the LSPR governed by interparticle resonances ($\bar{d}_p$ = 20 nm, $\bar{x}_s$ = 11 nm) was less sensitive to the thickness of TiO_2 on the Au surface (Figure 3), exhibiting a more moderate shift in peak wavelength from λ_{max} = 648 nm to λ_{max} = 680 nm as the TiO_2 thickness increased from 0.0 to 23 nm, although there was a pronounced broadening of the spectrum. The author notes that it is unlikely that such a small shift in the peak wavelength ($\Delta\lambda$ = 32 nm) was due to complete filling of the interparticle space after the deposition of 5.5 nm in the $\bar{d}_p$ = 20 nm, $\bar{x}_s$ = 11 nm case because 5.5 nm of TiO_2 resulted in a wavelength shift of $\Delta\lambda$ = 70 nm for the $\bar{d}_p$ = 15 nm, $\bar{x}_s$ = 19 nm case. The magnitude of the peak extinction for the LSPR governed by interparticle interactions ($\bar{d}_p$ = 20 nm, $\bar{x}_s$ = 11 nm) did increase with TiO_2 thickness, however, and the effect saturated after approximately 10 nm of TiO_2 (Figure 3). Both the close particle spacing ($\bar{x}_s$ = 11 nm) and the thick TiO_2 shell on the particles spaced farther apart ($\bar{x}_s$ = 19 nm) resulted in a shift of the peak wavelength to approximately 650 nm. Since both the particle−particle and particle−TiO_2 coupling results in approximately the same resonance frequency, a significant shift in λ_{max} was not observed for the closely spaced particles when coated by TiO_2. However, the

dx.doi.org/10.1021/cm2022467 |*Chem. Mater.* 2011, 23, 4612–4617

extinction coefficient did increase, which was expected considering an additional interaction was superimposed on the pre-existing particle−particle interaction. Indeed, the evolution of the extinction coefficient at λ_{max} with TiO_2 shell thickness in the closely spaced Au particles appeared to be the same as the particles spaced farther apart (Figure 4), offset by the initial extinction coefficient due to the interparticle coupling.

From the peak wavelength shift with TiO_2 thickness of the $\overline{d}_p$ = 15 nm, $\overline{x}_s$ = 19 nm case, and the magnitude of extinction increase of the $\overline{d}_p$ = 20 nm, $\overline{x}_s$ = 11 nm case, the sensing distances of the two different LSPR fields into the TiO_2 were estimated to be approximately 10 nm. A 10 nm sensing distance is further supported by the observation that the LSPR of 20 nm Au particles separated by 11 nm was dominated by interparticle resonances, while for 15 nm Au particles separated by 19 nm the LSPR was dominated by intraparticle resonances. It is noted that a 10 nm sensing distance is similar to that reported for the Ag−TiO_2 system,[28] and also similar to the approximate 8 nm maximum shell thickness reported for current enhancement in Ag−TiO_2 plasmon enhanced dye-sensitized solar cells.[9] It is somewhat surprising that less than 2.0 nm of TiO_2 did not result in a more significant shift in peak wavelength because the field enhancement is expected to be most intense near the particle surface, decaying exponentially with distance away,[34] but this observation could be due to delayed nucleation of TiO_2 on the Au surface (since the TiO_2 thickness was calculated based on the cycle numbers and average growth rate).

The substrate material and composition of the dielectric shell can alter the sensing distance. For SiO_2-coated 84 nm diameter Ag nanoparticles suspended in water, a sensing distance of 40 nm was observed.[29] In that case, the dielectric constant of SiO_2 at the peak LSPR wavelength of the Ag nanoparticles (512 nm) was 1.46, while the amorphous TiO_2 used in this study had a dielectric constant of 2.44 at the peak wavelength of 648 nm. The higher dielectric constant of TiO_2 would lead one to expect an attenuation of the LSPR-induced near field over a shorter distance in the case of TiO_2 compared to that of SiO_2, consistent with the observed shorter sensing distance in the present study. Another possibility is that the substrate played a role in dampening the field. For nanosized Ag strips on silicon surfaces, when illuminated, the localized field is preferentially focused into the silicon substrate, compared to air, illustrating how inhomogenaities in the dielectric environment could induce asymmetries in the field distribution.[37] Further experiments isolating the effects of the shell and substrate would help to experimentally clarify the roles of each component. It is expected that low-loss substrates and shells (e.g., quartz or SiO_2), would result in longer sensing distances.

CONCLUSION

A proof of concept was presented that aerosol deposition can be used to synthesize Au metal nanoparticles immobilized on a substrate with controlled size and separation distributions. The aerosol deposition concept is scalable and requires only a single step with deposition times in the range from 1 to 10 min. Samples were deposited where the LSPR was dominated by either intra- or interparticle resonances, and the effect of ultrathin TiO_2 shells in the thickness range from 0 to 24 nm on the UV−vis extinction spectra was measured. Results of changes in the UV−vis extinction spectra indicated a 10 nm sensing distance for the LSPR field away from the surface of these Au nanoparticles immobilized on FTO and coated with TiO_2.

EXPERIMENTAL DETAILS

Au nanoparticles were synthesized and deposited in a single step using a premixed FLAR (Figure 1), adapted from a system described in detail elsewhere.[17−19,30] The gold precursor was 13 mM $HAuCl_4$ (≥99.8% Fluka) dissolved in reagent grade ethanol (Sigma-Aldrich), which was fed into the flame using a nebulizer. The carrier gas (oxygen or argon) was supplied to the nebulizer at a pressure of 1.75 bar (SAFTEY NOTE: If an aerosol of ethanol is generated in oxygen, an explosive mixture is formed that can be easily ignited via flashbacks from the flame, resulting in a serious safety hazard), which according to the manufacturer's specifications resulted in a carrier gas flow rate of 1.6 liters per minute (lpm) and aerosol feed rate of 9.2×10^{-5} lpm, corresponding to an Au feed rate of 1.2 μmol/min. The combustion gas flow rates, controlled by digital mass flow controllers, were 0.58 lpm for CH_4 and 1.5 lpm for O_2, respectively. The combustion gases and aerosol stream from the nebulizer were mixed and passed through the burner, which consisted of a single nozzle with an outlet area of 0.08 cm^2. The flame temperature was not measured directly, but a system with similar geometry and flow rates corresponding to the case with argon carrier gas produced a temperature of 2200 K.[17]

The deposition substrate was F:SnO_2 (FTO, TEC 15, Pilkington Glass). The rms roughness of the FTO was 10.2 nm as measured by stylus profilometry using an Ambios XP1 Profilometer with a vertical resolution of 0.1 nm and lateral resolution of 100 nm. The measured rms roughness agreed well with the reported roughness of TEC 15 (10.3 nm) measured by AFM.[38] The substrate was positioned at a distance 16.0 cm away from the burner outlet, well above the luminous portion of the flame, and was thermally contacted to a water-cooled substrate holder via a small amount of thermal paste (Silver 5, Arctic Silver Inc.). The deposition time was varied from 4 to 12 min.

The size and separation distributions of the as-deposited Au nanoparticles on the substrates were determined from plan-view scanning electron microscope (SEM) images recorded in an FEI XLF30 operating at an accelerating voltage of 15 kV. The size distribution was determined by measuring the diameters of approximately 250 nanoparticles for a given sample. The separation distribution was determined by measuring the distance from the edge of a given nanoparticle to its nearest neighbors. Approximately 350 separation measurements were made per sample to obtain significant statistics. As noted above, the roughness of the FTO substrate introduces a systematic error in the 3D particle separation as measured from the 2D SEM images. The size and separation distribution parameters were obtained by fitting a log-normal distribution, which was the expected shape of the particle size distribution and also fitted the separation distribution.

Ultrathin films of TiO_2 were deposited on the FTO-supported Au nanoparticles by thermal atomic layer deposition (ALD) using a Savannah 100 (Cambridge Nanotech, Cambridge, MA) with titanium tetra-isopropoxide (TTIP) and water as the precursors. The deposition temperature was 200 °C and the ultra high purity N_2 flow rate was set to 10 standard cubic centimeters per minute (sccm). One A/B cycle consisted of a 0.1 s TTIP pulse (reservoir maintained at 80 °C) with a 2.0 s exposure time, followed by a 9.0 s N_2 purge, 0.015 s water pulse with a 2.0 s exposure time, and another 9.0 s purge. The growth rate of the TiO_2 was calibrated by depositing TiO_2 on 50 nm of thermally evaporated Au coated on optically polished silicon, and the average growth rate was found from elipsometric measurements to be 0.24 Å/cycle, very similar to the measured growth rate on the native oxide of polished silicon wafers (0.28 Å/cycle). The UV−vis extinction spectra were measured by transmission measurements in a diode array spectrometer (8452A, Hewlett-Packard) using a clean FTO substrate as the blank.

ASSOCIATED CONTENT

Supporting Information. Additional plots and calculations (PDF). This material is available free of charge via the Internet at http://pubs.acs.org.

AUTHOR INFORMATION

Corresponding Author
Phone: 612-655-7655. E-mail: ethimsen@anl.gov.

Present Addresses
Argonne National Laboratory, Material Science Division.

ACKNOWLEDGMENT

The author thanks S.C. Warren for helpful feedback on this manuscript and the European Commission for financial support (Project NanoPEC-Nanostructured Photoelectrodes for Energy Conversion, Contract Number 227179).

REFERENCES

(1) Kreibig, U.; Vollmer, M. *Optical properties of metal clusters*; Springer: Berlin, 1995.
(2) Nie, S. M.; Emery, S. R. *Science* **1997**, *275* (5303), 1102.
(3) Schuck, P. J.; Fromm, D. P.; Sundaramurthy, A.; Kino, G. S.; Moerner, W. E. *Phys. Rev. Lett.* **2005**, *94* (1), 017402.
(4) Ward, D. R.; Grady, N. K.; Levin, C. S.; Halas, N. J.; Wu, Y. P.; Nordlander, P.; Natelson, D. *Nano Lett.* **2007**, *7* (5), 1396.
(5) Ward, D. R.; Halas, N. J.; Ciszek, J. W.; Tour, J. M.; Wu, Y.; Nordlander, P.; Natelson, D. *Nano Lett.* **2008**, *8* (3), 919.
(6) Xu, H. X.; Aizpurua, J.; Kall, M.; Apell, P. *Phys. Rev. E* **2000**, *62* (3), 4318.
(7) Larsson, E. M.; Langhammer, C.; Zoric, I.; Kasemo, B. *Science* **2009**, *326* (5956), 1091.
(8) Adleman, J. R.; Boyd, D. A.; Goodwin, D. G.; Psaltis, D. *Nano Lett.* **2009**, *9* (12), 4417.
(9) Standridge, S. D.; Schatz, G. C.; Hupp, J. T. *J. Am. Chem. Soc.* **2009**, *131* (24), 8407.
(10) Thimsen, E.; Le Formal, F.; Graetzel, M.; Warren, S. *Nano Lett.* **2011**, *11*, 35.
(11) Nie, Z. H.; Petukhova, A.; Kumacheva, E. *Nature Nanotechnol.* **2010**, *5* (1), 15.
(12) Shevchenko, E. V.; Talapin, D. V.; Kotov, N. A.; O'Brien, S.; Murray, C. B. *Nature* **2006**, *439* (7072), 55.
(13) Liu, K.; Nie, Z. H.; Zhao, N. N.; Li, W.; Rubinstein, M.; Kumacheva, E. *Science* **2010**, *329* (5988), 197.
(14) Strobel, R.; Pratsinis, S. E. *J Mater. Chem.* **2007**, *17* (45), 4743.
(15) Strobel, R.; Baiker, A.; Pratsinis, S. E. *Adv. Powder Tech.* **2006**, *17* (5), 457.
(16) Mangolini, L.; Thimsen, E.; Kortshagen, U. *Nano Lett.* **2005**, *5* (4), 655.
(17) Thimsen, E.; Biswas, P. *AIChE J.* **2007**, *53* (7), 1727.
(18) Thimsen, E.; Rastgar, N.; Biswas, P. *J. Phys. Chem. C* **2008**, *112* (11), 4134.
(19) Biswas, P.; Thimsen, E. *Aerosol Measurements*, 3rd ed.; Wiley-VCH: New York, 2011; Chapter 33.
(20) Kulkarni, P.; Biswas, P. *J. Nanopart. Res.* **2003**, *5* (3−4), 259.
(21) Kulkarni, P.; Biswas, P. *Aerosol Sci. Technol.* **2004**, *38*, 541.
(22) Athanassiou, E. K.; Krumeich, F.; Grass, R. N.; Stark, W. J. *Phys. Rev. Lett.* **2008**, *101*, 16.
(23) Palgrave, R. G.; Parkin, I. P. *J. Am. Chem. Soc.* **2006**, *128* (5), 1587.
(24) Madler, L.; Stark, W. J.; Pratsinis, S. E. *J. Mater. Res.* **2003**, *18* (1), 115.
(25) Sotiriou, G. A.; Sannomiya, T.; Teleki, A.; Krumeich, F.; Voros, J.; Pratsinis, S. E. *Adv. Funct. Mater.* **2010**, *20* (24), 4250.
(26) Stark, W. J.; Luechinger, N. A.; Loher, S.; Athanassiou, E. K.; Grass, R. N. *Langmuir* **2007**, *23* (6), 3473.
(27) Hupp, J. T.; Hamann, T. W.; Martinson, A. B. F.; Elam, J. W.; Pellin, M. J. *J. Phys.Chem. C* **2008**, *112* (27), 10303.
(28) Standridge, S. D.; Schatz, G. C.; Hupp, J. T. *Langmuir* **2009**, *25* (5), 2596.
(29) Evanoff, D. D.; White, R. L.; Chumanov, G. *J. Phys. Chem. B* **2004**, *108* (5), 1522.
(30) Thimsen, E.; Biswas, S.; Lo, C. S.; Biswas, P. *J. Phys. Chem. C* **2009**, *113* (5), 2014.
(31) Tsai, H. C.; Hu, E.; Perng, K.; Chen, M. K.; Wu, J. C.; Chang, Y. S. *Surf. Sci.* **2003**, *537* (1−3), L447.
(32) Hinds, W. C., *Aerosol technology: properties, behavior, and measurement of airborne particles*, 2nd ed.; Wiley: New York, 1999.
(33) Friedlander, S. K. *Smoke, dust, and haze: fundamentals of aerosol dynamics*, 2nd ed.; Oxford University Press: New York, 2000.
(34) Jain, P. K.; Huang, W. Y.; El-Sayed, M. A. *Nano Lett.* **2007**, *7* (7), 2080.
(35) Tricoli, A.; Righettoni, M.; Krumeich, F.; Stark, W. J.; Pratsinis, S. E. *Nanotechnology* **2010**, *21*, 46.
(36) Link, S.; El-Sayed, M. A. *J. Phys. Chem. B* **1999**, *103* (21), 4212.
(37) Pala, R. A.; White, J.; Barnard, E.; Liu, J.; Brongersma, M. L. *Adv. Mater.* **2009**, *21* (34), 3504.
(38) Hu, Z. Y.; Zhang, J. J.; Hao, Z. H.; Hao, Q. Y.; Geng, X. H.; Zhao, Y., *Appl. Phys. Lett.* **2011**, *98*, (12).